

Strengthening and toughening mechanisms in Mg–Zn–Y alloy with a long period stacking ordered structure

X.H. Shao^{a,b}, Z.Q. Yang^{a,*}, X.L. Ma^{a,**}

^a Shenyang National Laboratory for Materials Science, Institute of Metal Research, Chinese Academy of Sciences, Shenyang 110016, People's Republic of China

^b Graduate School of Chinese Academy of Sciences, Beijing 100049, People's Republic of China

Received 14 August 2009; received in revised form 24 March 2010; accepted 4 May 2010

Abstract

The deformation behavior and corresponding microstructure evolution of a Mg₉₇Zn₁Y₂ (at.%) alloy with a long period stacking ordered (LPSO) structure subjected to hot compression were investigated. The peak stress at 573 K was about 190 MPa, and no macroscopic fracture took place up to a strain of about 60%. The mechanisms responsible for the mechanical performance of the Mg₉₇Zn₁Y₂ (at.%) alloy are discussed based on microstructural investigations using various electron microscopy techniques. The high strength at elevated temperature could be attributed to synergetic strengthening refinement of the LPSO via kinking and a limited fraction of dynamical recrystallization. Microcracks nucleated at the interfaces in the sandwich structure composed of LPSO and nanometer thick Mg slices could weaken the alloy at late stages of deformation, but their propagation could be limited within the individual kink band where the microcracks nucleated, which could ensure the capability of the alloy to resist premature or catastrophic fracture. Furthermore, lack of deformation twins in Mg grains effectively reduced the potential nucleation sites for cracks, which should be another reason for the good ductility of the alloy. These findings may provide or evoke insights into methods for optimizing the mechanical properties of Mg alloys.

© 2010 Acta Materialia Inc. Published by Elsevier Ltd. All rights reserved.

Keywords: Mg–Zn–Y alloy; Long period stacking ordered structure; Kinking; Strengthening; Toughening

1. Introduction

Magnesium alloys are attractive as light weight structural materials owing to their low density, high specific strength, good damping and ease of recycling, which can be used in lots of areas, including automobiles, hand tools, sports equipment, electronic equipment and aerospace applications [1]. However, low strength and poor ductility hinder their widespread application. Therefore, great effort has been expended to improve the strength and ductility of Mg alloys.

Recently a new nanocrystalline Mg₉₇Zn₁Y₂ (at.%) alloy which exhibited a high thermal stability and superior mechanical properties with a tensile yield strength of ~600 MPa and elongation of ~5% at room temperature was produced by rapidly solidified powder metallurgy processing [2,3]. These excellent properties seem to originate not only in grain refinement but also a novel precipitate with a long period stacking ordered (LPSO) structure [4]. It was demonstrated that this phase is a long period chemical and stacking ordered structure by high angle annular dark field scanning transmission electron microscopy (HAADF STEM). Thereafter, various LPSO phases of 10H, 14H, 18R and 24R types have been observed in several kinds of ternary Mg–Zn–RE (rare earth) systems [5–8]. Notably, the formation of LPSO structure in Mg alloys was found to maintain the yield and ultimate

* Corresponding author.

** Corresponding author.

E-mail addresses: yangzq@imr.ac.cn (Z.Q. Yang), xlma@imr.ac.cn (X.L. Ma).

strength at 473 K at basically the same level as at room temperature [9], which was not observed in Mg alloys consisting of other kinds of precipitates. Therefore, Mg alloys containing an LPSO phase may be one potential structural material for elevated temperature applications. Some hardening or strengthening effects of the LPSO phase on Mg grains have been reported for Mg alloys containing LPSO structure. $\langle c + a \rangle$ dislocations were observed in Mg grains with LPSO precipitates, instead of $\langle a \rangle$ dislocations on the basal plane [10]. The result implies that the formation of an LPSO phase increases the critical resolved shear stress of the basal slip and activates non-basal slip in the Mg matrix, which is supported by first principle calculations [11]. Also, $\{10\bar{1}2\}$ deformation twins in the Mg matrix are prevented by the profuse LPSO phase in rapidly solidified $\text{Mg}_{97}\text{Zn}_1\text{Y}_2$ (at.%) alloys [12]. As for deformation of the LPSO phase itself, kink bands were observed within the LPSO structure in Mg–Zn–RE alloys [13–16]. Lately, Hagihara et al. [13,14] reported that the plastic behavior of the Mg_{12}ZnY LPSO phase is highly anisotropic. Deformation kinks were initiated in the alloy and to some extent accommodated the compressive strain when stress was loaded parallel to the (0 0 0 1) plane, in which case the Schmid factor for basal slip is negligible. They stressed that kink deformation is an essential mechanism to generate homogeneous strain in crystals and that it contributes to some extent to the ductility. However, the effect of kinking of the LPSO phase on the deformation behavior and mechanical properties of Mg alloys with LPSO structure is still unclear. Therefore, it is necessary to investigate the mechanism of deformation kinking in the LPSO phase in Mg alloys at the atomic level and, especially, its influence on the deformation behavior and mechanical properties of the Mg alloys. It is the aim of this study to reveal the microscopic mechanisms of the LPSO phase on strengthening and toughening of a $\text{Mg}_{97}\text{Zn}_1\text{Y}_2$ (at.%) alloy, which might shed new light on optimizing the mechanical properties of Mg alloys by distinctive microstructures.

2. Experiments

Samples with the nominal composition $\text{Mg}_{97}\text{Zn}_1\text{Y}_2$ (at.%) were prepared from high purity a Mg, Zn and Mg–25Y (wt.%) master alloy by high frequency induction melting in a graphite crucible at approximately 1023 K under an argon atmosphere. Specimens with the dimensions $4 \times 4 \times 8 \text{ mm}^3$ were cut from the ingots by electrical discharge machining. Microhardness was measured in a MVK-H300 Vickers hardness testing machine, with a load of 50 g and a loading time of 10 s. Hot compression experiments were carried out at 573 K and a strain rate of $1.0 \times 10^{-3} \text{ s}^{-1}$ in a Gleeble-1500 thermal simulation machine. Prior to being compressed the specimens were conductively heated to 573 K at a heating rate of 5 K s^{-1} and held for 180 s for equilibration. The compression direction was parallel to the long axis of the specimens. Some tests were stopped when the specimens were deformed to

peak strains of $\sim 23\%$ and 60% without failure, then immediately water quenched to room temperature for microstructure analysis. The microstructures of the samples parallel to the compression axis were observed by scanning electron microscopy (SEM) and transmission electron microscopy (TEM). Thin foil samples for TEM were prepared by the conventional ion milling method. A Tecnai G² F30 microscope, operated at 300 keV and equipped with an HAADF detector, was used for microstructure analysis.

3. Results

3.1. True stress–true strain curve

The compression stress–strain curve of the $\text{Mg}_{97}\text{Zn}_1\text{Y}_2$ alloy under a strain rate of $1.0 \times 10^{-3} \text{ s}^{-1}$ at 573 K is shown in Fig. 1, which can be divided into three stages, OA, AB and BC. Initially the stress increased almost linearly in stage OA. In stage AB the stress continued to increase to a peak stress of about 190 MPa at a strain of about 23%, but the work hardening rate decreased continuously with increasing strain. Finally, the stress decreased slightly with increasing strain in stage BC, indicating a slight and slow work softening. The yield and peak stresses at 573 K were about 90 and 190 MPa, respectively. Samples with different applied strains (B, 23%; C, 60%) were selected for microstructural investigations, which hereafter are referred to as sample B and sample C, respectively.

3.2. Microstructure of $\text{Mg}_{97}\text{Zn}_1\text{Y}_2$ cast alloy

Fig. 2 is a back-scattered electron (BSE) SEM image of the $\text{Mg}_{97}\text{Zn}_1\text{Y}_2$ cast alloy, showing a duplex microstructure. The phase with bright contrast in the BSE SEM image was enriched in Zn and/or Y, compared with the dark contrast phase of the Mg matrix. The secondary phase, 5–35 μm in thickness, formed a three-dimensional quasi-continuous honeycomb-like network at Mg grain boundaries. The Mg

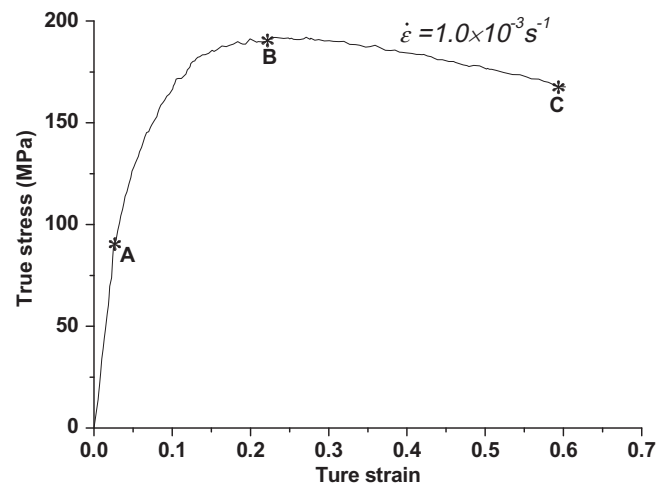


Fig. 1. True stress–true strain curves obtained from compression tests at 573 K under a constant strain rate of $1.0 \times 10^{-3} \text{ s}^{-1}$.

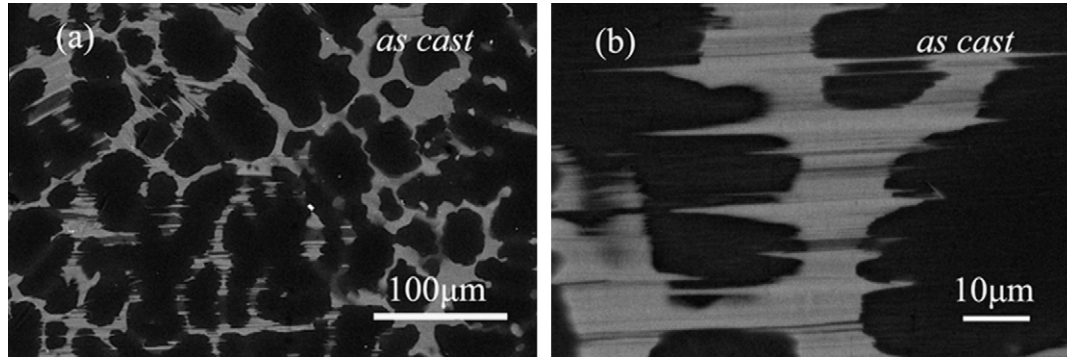


Fig. 2. BSE SEM image of the $Mg_{97}Zn_1Y_2$ cast alloy at (a) low and (b) high magnification, respectively, showing the morphology of the secondary phase and Mg grains.

grains were estimated to be about 100 μm wide. Fig. 2b is a magnified image of the second phase. It was found that bright and gray lamellae of different thicknesses alternated with each other in the secondary phase network, which

should be LPSO phases, similar to those reported in Mg–Zn–RE systems [6,7,9]. The microhardness of Mg grains and the secondary phase in the $Mg_{97}Zn_1Y_2$ cast alloy were 70.3 ± 6.9 and 77.8 ± 4.7 , respectively. This indicates that the secondary phase was a little harder than the Mg matrix.

Fig. 3a is a bright field TEM image of the boundaries, including the bright and gray lamellae within the secondary phase in the $Mg_{97}Zn_1Y_2$ cast alloy. The corresponding selected area electron diffraction (SAED) patterns recorded along the $\langle 11\bar{2}0 \rangle_{Mg}$ direction for the regions marked B and C in Fig. 3a are shown in Fig. 3b and c, respectively. In the SAED pattern shown in Fig. 3b there are weaker spots at positions $n/6$ (where n is an integer) of the $(0002)_{Mg}$ diffraction. This shows that the phase in area B is a 18R-LPSO phase [6,7]. No periodic extra spots but streaking parallel to the $[0002]_{Mg}$ direction can be observed in the SAED pattern shown in Fig. 3c. The phase in area C is thus considered the commonly accepted 2H–Mg with lots of stacking faults (SFs) [4–6,17–20], which might be different from the precipitates in Mg–1Gd–0.4Zn–0.2Zr alloy [21]. Analytical TEM analysis shows that there is segregation of Zn/Y on the SFs, which will not be discussed in the present report. The spot at $1/2$ of $(0002)_{Mg}$ arises from double diffraction. Fig. 3d is a high resolution TEM (HR TEM) image of the 18R-LPSO phase viewed along the $\langle 11\bar{2}0 \rangle_{LPSO}$ direction, showing the stacking sequence ABA-BABCACACABCBCBC. Fig. 3e is a high resolution HAADF STEM image of the LPSO phase viewed along the $\langle 11\bar{2}0 \rangle_{LPSO}$ direction. The heavier Zn and/or Y atoms are distributed periodically at two adjacent basal planes in the LPSO structure. The present results are consistent with other data for $Mg_{97}Zn_1Y_2$ alloys [4,5,18,22]. Therefore, the boundaries in the $Mg_{97}Zn_1Y_2$ cast alloy are composed of mainly 18R-LPSO phase and some Mg segments and correspond to the bright and gray lamellae in the BSE SEM image (Fig. 2b), respectively.

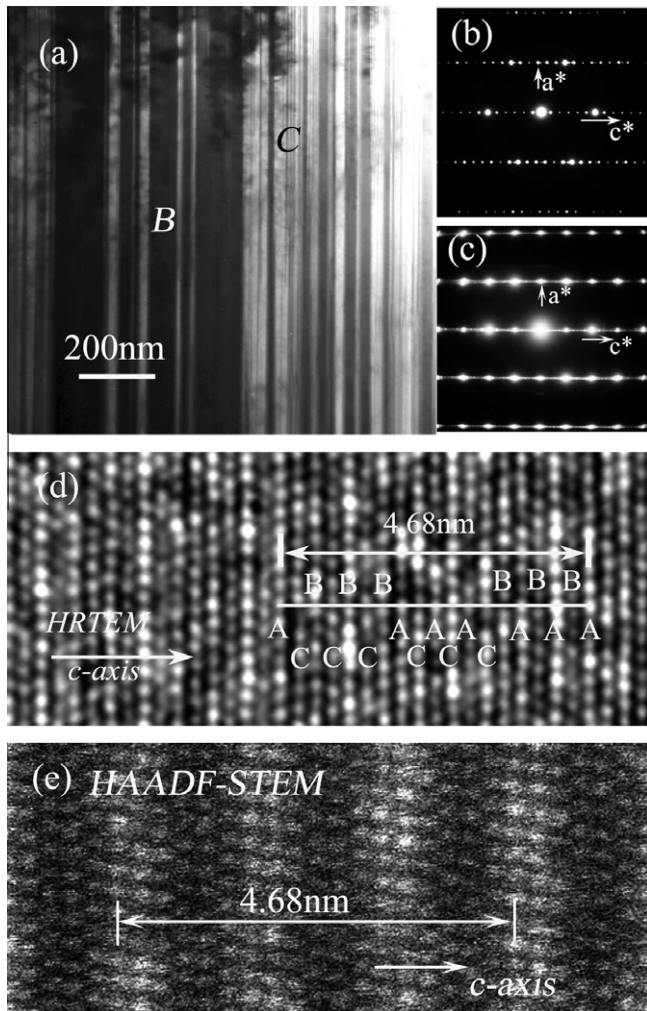


Fig. 3. (a) TEM image of the boundary in the $Mg_{97}Zn_1Y_2$ cast alloy. (b and c) SAED patterns recorded along the $\langle 11\bar{2}0 \rangle_{Mg}$ direction for the areas marked B and C in (a), respectively. (d and e) HR TEM and HAADF STEM images, respectively, revealing the stacking ordered as well as chemically ordered LPSO structure.

3.3. Deformation microstructure in the LPSO phase

3.3.1. Kinking of the LPSO phase

Fig. 4 shows BSE SEM micrographs of samples B and C. The Mg grains are elongated along directions normal

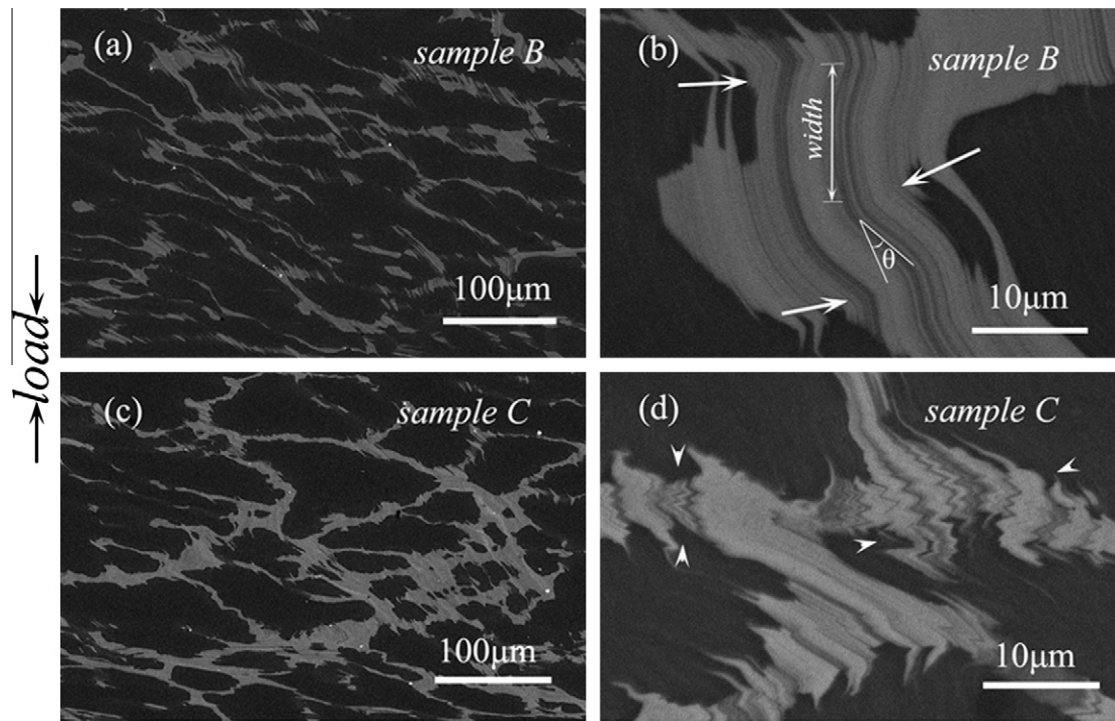


Fig. 4. (a and c) Low magnification BSE SEM images of samples B and C, respectively. (b and d) High magnification images of kink bands in samples B and C, respectively. The kink boundaries are indicated by white arrows and multiple kink bands are denoted by pairs of white arrowheads. The compression axis is denoted at the left of Fig. 4. The kinking angle θ is defined in Fig. 4b.

to the loading axis in both samples B (Fig. 4a) and C (Fig. 4c), compared with the $\text{Mg}_{97}\text{Zn}_1\text{Y}_2$ cast alloy (Fig. 2a). Furthermore, from high magnification SEM observations it can be seen that kink bands are formed in the LPSO phase in both samples B and C, as shown in Fig. 4b and d, respectively. The width of the kink bands was mostly of the order of $10\ \mu\text{m}$ and the kinking angles θ were less than 30° in sample B, as indicated by the white arrows in Fig. 4b (hereafter the corresponding kink boundaries (KBs) are referred to as low angle KBs). When the strain increased to 60% (sample C) the kinking angles mostly increased to values higher than 30° (hereafter the corresponding KBs are referred to as high angle KBs). Multiple kinking of the LPSO phase occurred in sample C and the width of the kink bands was much less than $10\ \mu\text{m}$, forming a fine serrated structure consisting of high angle KBs (indicated by arrowheads in Fig. 4d). This indicates that not only new kinks were formed within former kink bands, but also that the kinking angles increased in the LPSO phase as the strain increased. In addition, there were no cracks large enough to be observed within the kinked LPSO phase or at interfaces between the LPSO structure and bulk Mg grains even in the higher magnification SEM images (Fig. 4b and d). The Vickers microhardnesses of the Mg grains and LPSO phase in samples B and C were about 85.8 ± 4.1 and 100.1 ± 2.8 and 89.4 ± 1.7 and 112.0 ± 6.3 , respectively. Obviously, both Mg grains and the LPSO phase in samples B and C were harder than those in the as cast alloy, as a result of work hardening.

In order to understand the atomic scale mechanism of kinking of the LPSO phase, TEM and HR TEM investigations were carried out. Fig. 5a is a TEM image of a kinked LPSO structure in sample B. The KBs look relatively sharp and flat. SAED analysis showed that the basal planes of the kink bands on both sides of the left KB rotated around a $\langle 1\bar{1}00 \rangle_{\text{LPSO}}$ zone axis by about 15° relative to each other (inset in Fig. 5a). Fig. 5b and c are HR TEM images of the left and right KBs, respectively. Fast Fourier transform (FFT) analysis of the HR TEM images demonstrated that these two KBs were composed of basal edge dislocations with a Burgers vector $b = 1/3 \langle 11\bar{2}0 \rangle_{\text{LPSO}}$, as designated by “T”. The mean distance between adjacent dislocations was about $6.2\ \text{\AA}$, from which a tilt angle $\theta \approx 15^\circ$ was calculated, which is consistent with the SAED results. It can be observed that the dislocations of the left and right KBs were of opposite sign (Fig. 5b and c), i.e. the low angle kink bands were bounded by opposite “tilt walls” of dislocations.

Fig. 6 is a TEM image of faceted KBs in sample B. There are some small steps along the KBs at the intersection of KBs and nanometer thick Mg slices (hereafter referred to as Mg nano-slices) embedded or sandwiched in between LPSO blocks, as indicated by the white arrowheads in Fig. 6a. HR TEM observations demonstrated that the faceted KBs between the LPSO sub-bands were also composed of basal $1/3 \langle 11\bar{2}0 \rangle_{\text{LPSO}}$ dislocations. However, HR TEM analysis of the faceted area marked “B” shows that the dislocations in the Mg nano-slice were

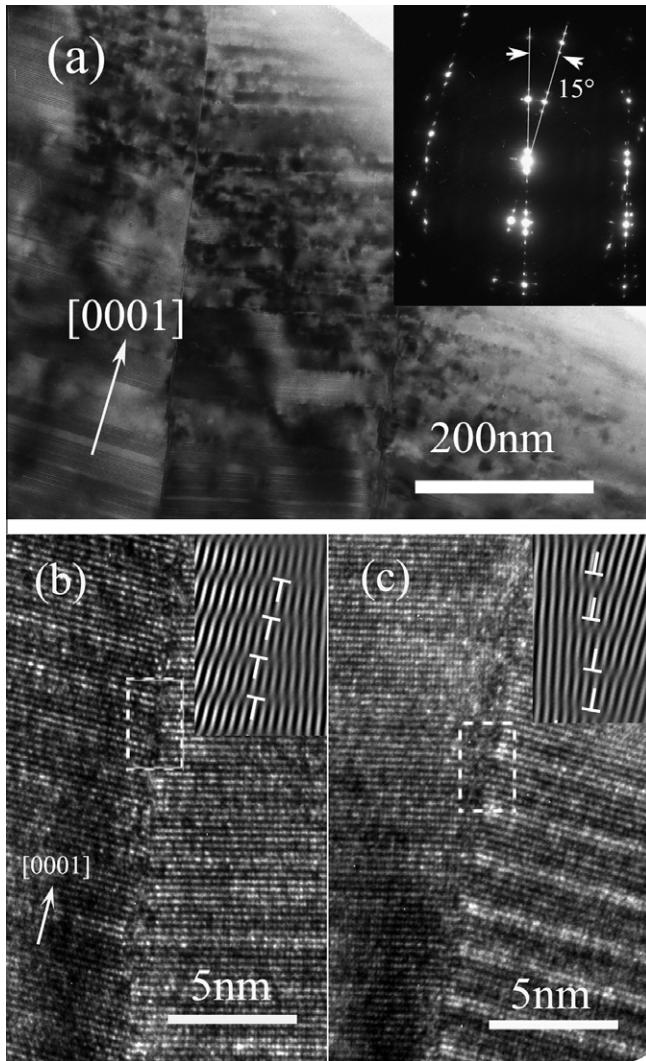


Fig. 5. (a) TEM micrograph of kink bands with sharp and flat KBs in the LPSO in sample B, viewed in the $\langle 1\bar{1}00 \rangle_{\text{Mg}}$ direction. The SAED pattern of the left KB is shown in the insert to (a). (b and c) HR TEM images of the left and right KBs, with FFT results as insets for the dashed rectangles, respectively. Dislocations are designated by “T”.

$1/2[0001]_{\text{Mg}}$ prismatic dislocations, as shown in Fig. 6b. Formation of the prismatic dislocations in the Mg nano-slices, and the relation to the faceted KBs, could be understood as follows. The softer Mg nano-slice could be sheared along the kinking direction via prismatic slip of $1/2[0001]_{\text{Mg}}$ dislocations by the harder LPSO kink bands, instead of activating basal slip, resulting in a dislocation wall deviating from the KB. Kinking of the next LPSO lamella would then nucleate at the intersection between the LPSO phase–Mg nano-slice interface and the inclined dislocation wall in the Mg nano-slice, resulting in the appearance of faceted KBs. Fig. 6c is an FFT analysis of the HR TEM image, using $\{11\bar{2}0\}_{\text{LPSO}}$ type reflections, for the LPSO area near the tip of the kink band marked “C” in Fig. 6a, which clearly shows the existence of dislocations with Burger’s vectors of opposite sign in area C. Hereafter, dislocations with Burger’s vectors of opposite sign are referred to as L and R dislocations, respectively,

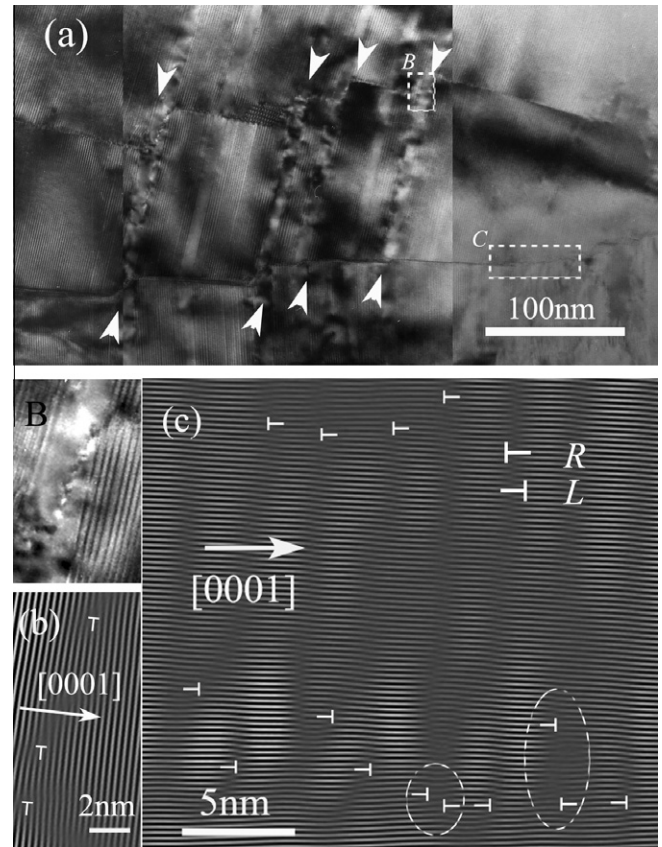


Fig. 6. (a) TEM image of kink bands with faceted KBs in the LPSO phase in sample B. Panel B is an enlargement of area B in (a). (b) FFT image of area B in (a) filtered for $\{0001\}_{\text{Mg}}$ type reflections, showing the prismatic dislocations in Mg. (c) FFT image of area C in (a) filtered for $\{11\bar{2}0\}_{\text{LPSO}}$ type reflections, showing dislocations near the kink band tip.

as indicated in Fig. 6c. The KB near the kink tip was composed of dislocations distributed in a band several nanometers wide, which shows a non-equilibrium high energy state. Dislocations within the KB region were mainly of L type, however, two R dislocations could be identified very close to the tip, which were in the form of dislocation pairs with L dislocations, as indicated by the dotted ellipses in Fig. 6c. An array of R dislocations could be observed in the upper LPSO kink band, about 20 nm away from this KB. L and R dislocations will glide in opposite directions under shear stress. The above results imply that kinking of the LPSO phase is closely related to the generation and synchronized slip of dislocation pairs of opposite sign on basal planes during compression. The high energy faceted KBs (Fig. 6) were converted to low energy flat KBs (Fig. 5) via movement and rearrangement of dislocations.

Kinking, as first reported by Orawan [23], is a deformation mode typically observed in hexagonal metals such as Zn and Cd. The origin of deformation kinking in the LPSO phase has been reported to result from a progressive rotation of the lattice by avalanche generation of pairs of dislocations on the basal plane [13,14]. Based on our HR TEM observations (Figs. 5 and 6), the synchronized slip of

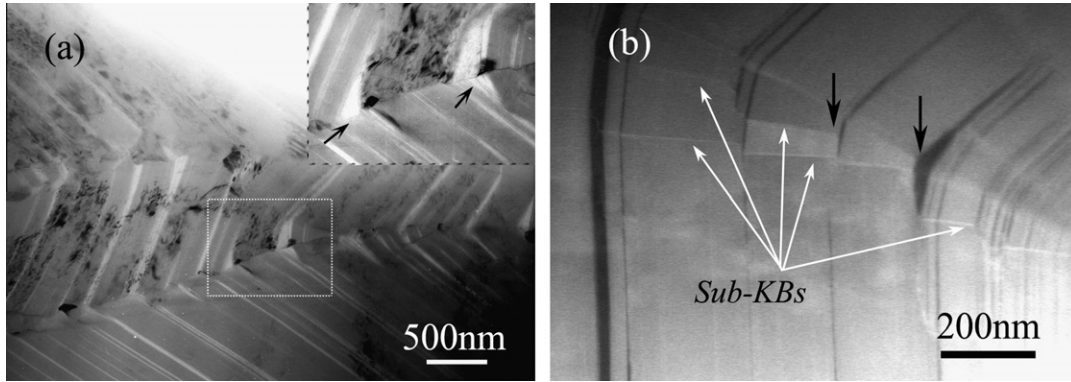


Fig. 7. (a) TEM image of kink bands with high kinking angles in the LPSO phase in sample C. It is obvious that microcracks nucleate at the high angle KBs and propagate along basal planes, shown by the inset in (a) (indicated by black arrows). (b) Low magnification STEM image of kink bands with sub-KBs (denoted by white arrows).

dislocations mechanism of kinking [24,25] was confirmed at the atomic scale.

Fig. 7 shows the microstructure of the kinked LPSO phase in sample C. It is apparent that multiple kink bands in the LPSO phase are associated with high kinking angles in sample C, which is consistent with the SEM observations (Fig. 4d). In addition to the primary high angle KBs in sample C, some low angle sub-KBs were observed in some regions, as indicated by the white arrows in Fig 7b. Additionally, nucleation of microcracks was found at the high angle KBs in sample C, as indicated by the black arrows in Fig. 7, which will be presented in detail in the next section.

3.3.2. Microcracks

In addition to the multiple kink bands in the LPSO phase of sample C, TEM observations show that there were triangular voids at the high angle KBs, which could be microcracks, as indicated by the black arrows in Fig. 7a and b. These microcracks were mostly formed at the intersection of high angle KBs and the interfaces between the LPSO structures and Mg nano-slices embedded or sandwiched in between LPSO blocks. However, no microcracks were observed in the kinked LPSO blocks with wider kink bands and lower kinking angles ($<30^\circ$) in sample B. This indicates that nucleation of microcracks at KBs along the interfaces between the LPSO phase and the embedded or sandwiched Mg nano-slices might take place when the kinking angle increases to a threshold value during deformation. It seems that the microcracks could propagate into the kink band along basal planes, according to the shape of the microcracks. The dark triangular region indicated by the black arrow in Fig. 7b was found to be thinner than its neighboring regions by analytical TEM analysis, which demonstrates that local necking took place, which would develop into a microcrack with further straining. Propagation of the necked regions, i.e. microcracks, was hampered by sub-KBs, denoted by the white arrows in Fig. 7b. It can be expected that local cleavage would occur once a microcrack propagated across a kink band within the LPSO

phase, however, cleavage could be confined temporarily within the kink band, since the basal planes of the next kink band would be deflected from the microcrack propagation direction due to the formation of high angle KBs.

3.4. Deformation microstructure in bulk Mg grains

Fig. 8 shows a TEM image of an interface region consisting of large Mg grains coherent with the LPSO kink bands at basal planes in the deformed samples. It is apparent that the KBs in the LPSO phase were transferred to the adjacent bulk Mg grains without any deviation, resulting in the appearance of a grain boundary (GB) in Mg having the same tilt angle, which is different from the deformation of a Mg nano-slice between two LPSO lamellae (Fig. 6). HR TEM observations demonstrated that a GB in a Mg grain, shown in Fig. 8 by a dashed line, is composed of dislocations, as are the KBs in the LPSO phase (Fig. 5). Thus, the formation of such tilt GBs in Mg is also a result of the generation and synchronized slip of basal dislocation pairs with opposite signs, and, therefore, the new GBs formed by deformation kinking in the Mg grains will hereafter be termed kink GBs, in order to emphasize their dependence on kinking of the neighboring LPSO phase.

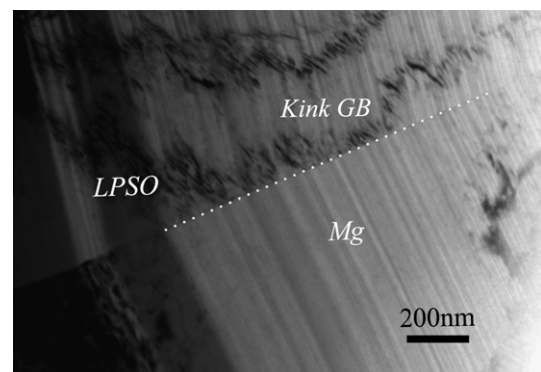


Fig. 8. TEM image of an interface region consisting of Mg grains coherent with the LPSO phase kink bands.

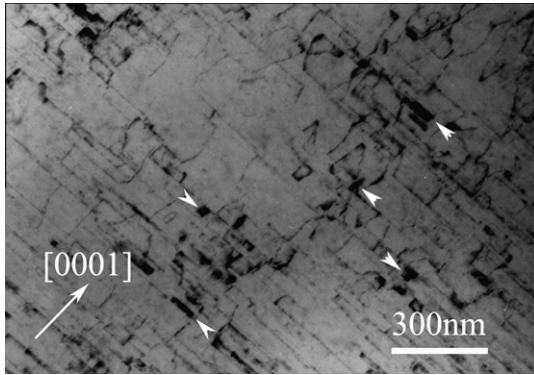


Fig. 9. TEM image showing dislocations in Mg grains far from the LPSO phase–Mg matrix interface in sample C.

Fig. 9 is a TEM image of Mg grains far from the LPSO phase in sample C. There are lots of SFs on the basal planes. Dislocations are mostly observed within Mg bands between two adjacent SFs and are bounded by the SFs. It is thus suggested that the dislocations shown in Fig. 9 are not on the basal planes of Mg. In addition, the SF planes are not sheared along the $[0001]_{\text{Mg}}$ direction. Therefore, only prismatic and/or pyramidal slip occurred in this Mg grain during deformation. This shows that the basal SFs play an important role in impeding the glide of dislocations along directions such as $[0001]_{\text{Mg}}$ and $\langle 11\bar{2}3 \rangle_{\text{Mg}}$. The appearance of small darker regions (indicated by white arrowheads) shows the formation of small areas with a large strain concentration or even local lattice rotation, resulting in a contrast different from the surrounding Mg, which should be an indication of sub-structures of dynamic recrystallization (DRX). The dynamically recrystallized Mg grains may have the same thickness as the original Mg bands separated by dense SFs in the matrix. This can be easily understood, since the dislocation motion was limited within the Mg bands between two adjacent SFs.

Fig. 10a and b shows typical optical micrographs of samples B and C, respectively, indicating that there is no obvious DRX in the Mg grains, which is different from the situation of the extruded $\text{Mg}_{97}\text{Zn}_1\text{Y}_2$ alloy at higher temperatures [26]. The deformation kinks are indicated

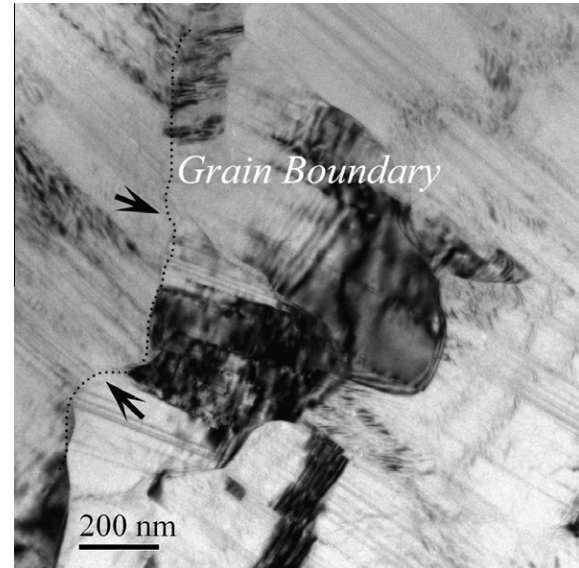


Fig. 11. TEM image showing a wavy and corrugated grain boundary in the Mg matrix.

by arrows in Fig. 10. Closer TEM observations found a few recrystallized grains at some wavy and corrugated grain boundaries in the Mg matrix, as shown in Fig. 11. This shows local migration of high angle GBs via DRX in Mg grains during plastic deformation [27]. In addition, the relative rotation and shear of SFs (see arrows in Fig. 11) on both sides of the GB indicates that local lattice rotation and GB sliding accompanied the migration of boundaries during deformation. The SFs in the Mg grains were not recovered during DRX, which could be due to segregation of Zn/Y on the SFs. TEM observations demonstrated that no extensive DRX occurred during hot compression, which is consistent with the optical observations (Fig. 10).

Twinning is frequently observed in deformed Mg and its alloys [28,29]. However, twinning in Mg grains was rarely observed in this work. This may result from the elevated temperature and/or lower strain rate. Fig. 12 shows a $\{10\bar{1}2\}$ twin band in a Mg grain. There are lots of SFs

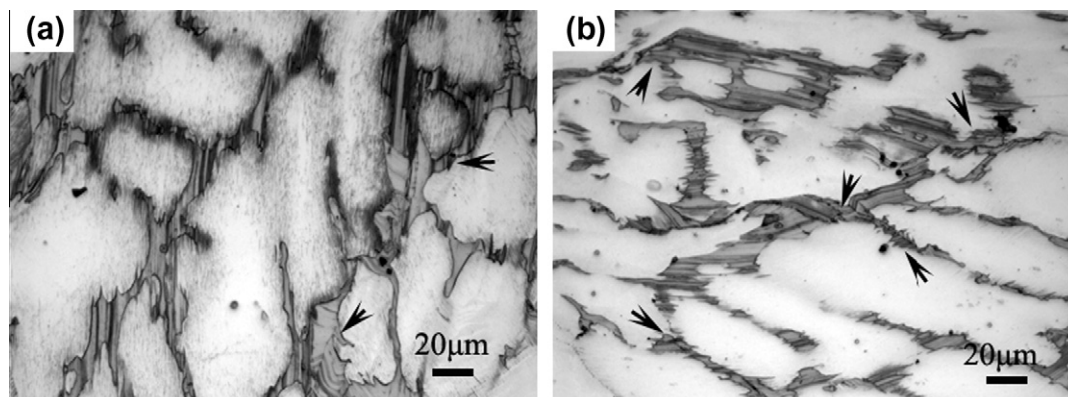


Fig. 10. Optical micrographs showing the scarce occurrence of DRX of Mg in samples B (a) and C (b).

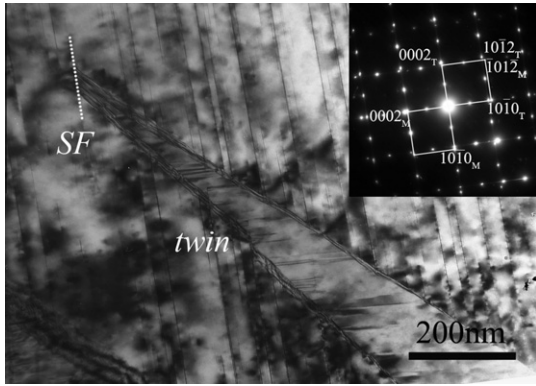


Fig. 12. TEM image showing the interaction between SFs and the deformation twin, with the SAED pattern of the twin as an inset.

with segregation of Zn/Y in the Mg grains. The twinning band ended at a SF, as indicated by the dashed line in Fig. 12, indicating that SF can prevent the growth of twins. This might be another reason for the lack of twins in the $\text{Mg}_{97}\text{Zn}_1\text{Y}_2$ alloy, which is consistent with the results for rapidly solidified Mg alloys [12].

3.5. Coherent interfaces between the LPSO phase and bulk Mg grains

HR TEM observations showed that the LPSO phase–Mg matrix interface was coherent along both the basal and prismatic planes in the $\text{Mg}_{97}\text{Zn}_1\text{Y}_2$ cast alloy, as expected. Fig. 13a shows a TEM image of the LPSO phase–Mg matrix interface region in sample C, which is denoted by the black dotted line. There were apparently no voids or cracks along the interface. Fig. 13b shows an HR TEM image of the interface region in the square in Fig. 13a. The basal interface was still coherent, flat and sharp, as in the as cast state. The prismatic interface became faceted, as indicated by the white dotted curve,

but still coherent. Any debonding or nanoscale defect at the LPSO phase–Mg matrix interface region could not be seen in Fig. 13b.

4. Discussion

From the above electron microscopy observations it can be concluded that the morphology of the LPSO phase underwent significant changes, with deformation kinking, during hot compression. Not only can the harder LPSO structure itself serve as a strengthening phase in the $\text{Mg}_{97}\text{Zn}_1\text{Y}_2$ alloy, but other microstructural factors, including the LPSO phase–Mg matrix coherent interface, KBs, dislocations and microcracks in the LPSO phase may also play a vital role in determining the mechanical properties of the $\text{Mg}_{97}\text{Zn}_1\text{Y}_2$ alloy.

4.1. Effect of the LPSO structure and coherent interfaces between the LPSO phase and bulk Mg grains

$\text{Mg}_{97}\text{Zn}_1\text{Y}_2$ alloys have excellent mechanical properties [2–4,18] owing to the LPSO phase, which can increase biocompatibility with an increase in elastic modulus and hardness and preservation of high ductility [5]. From the morphology of the as cast $\text{Mg}_{97}\text{Zn}_1\text{Y}_2$ alloy (Fig. 2) it can be speculated that the three-dimensional quasi-continuous honeycomb-like structure formed by the harder LPSO phase can be considered a stronger skeleton, which can improve the ability to resist compression of the bulk material. In addition, hardening due to dislocation piling-up and pinning at the LPSO phase–Mg interface should not be neglected, since there are structural and chemical differences between the LPSO phase and α -Mg solid solution.

The interface between the LPSO phase and bulk Mg grains is one of the important factors influencing the mechanical properties of the alloy. Here we would like to

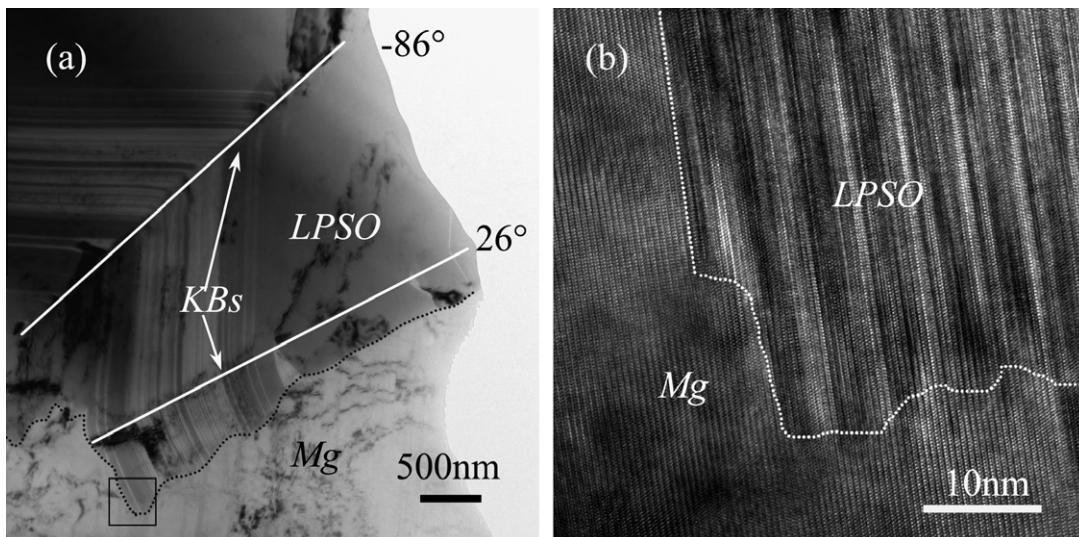


Fig. 13. (a) TEM image of the LPSO phase–Mg matrix interface region in sample C, which is denoted by a dotted curve. (b) HR TEM image of the region enclosed by a square in (a).

emphasize that by Mg grains we refer to large ones with sizes of or over several tens of micrometers, rather than the Mg nano-slices embedded or sandwiched in between LPSO blocks. Fig. 13 shows that there were apparently no voids or cracks along the coherent interface between the LPSO phase and bulk Mg grain. This is completely different to the case of interfaces between the LPSO structure and Mg nano-slices embedded or sandwiched between LPSO blocks, where microcracks nucleated during kinking of the LPSO phase (Fig. 7), i.e. coherent interfaces between the LPSO phase and bulk Mg grains were not favored nucleation sites for voids and/or microcracks during deformation, since no debonding or nano-scale defects (voids or microcracks) were detected at the atomic level (Fig. 13b). The stability of the LPSO phase–bulk Mg grain interface in the $Mg_{97}Zn_1Y_2$ alloys is important for the strength and ductility of the alloy.

4.2. Effect of kinking of the LPSO phase on strength and ductility of the alloy

Coarsening of the secondary phase will usually impair the strength of materials working at elevated temperatures, which can cause catastrophic failure. Synchronized slip of perfect dislocation pairs took place on the basal planes in the LPSO phase during compression, resulting in kinking of the LPSO phase (Figs. 4–7). Large LPSO blocks were transformed into small kink bands due to this kinking, which resulted in refinement rather than coarsening of the LPSO phase. The microhardness measurements showed that kinking resulted in a corresponding hardening of the LPSO region, as shown in Table 1. Kinking of the LPSO phase is thus expected to strengthen the alloy according to the Hall–Petch relationship. Therefore, besides LPSO phase–Mg matrix interfacial strengthening, kinking of the LPSO structure should also contribute to the work harden-

Table 1
Summary of microhardness of Mg and LPSO in the as cast sample, samples B and C, respectively.

| | Mg grain | LPSO |
|----------|-------------|--------------|
| As cast | 70.3 ± 6.93 | 77.8 ± 4.65 |
| Sample B | 85.8 ± 4.09 | 100.1 ± 2.79 |
| Sample C | 89.4 ± 1.68 | 112.0 ± 6.34 |

Table 2
Comparison of the peak stresses of the Mg alloys tested in hot compression at 573 K.

| Mg alloy | Peak stress (MPa) | Strain rate ($\times 10^{-3} s^{-1}$) | Reference |
|------------------------------|-------------------|---|---------------|
| Pure Mg | 30 | 1.7 | [30] |
| Mg–0.035 at.% Ce | 60 | 1.7 | [30] |
| AZ31 | 42 | 1.0 | [31] |
| AZ91 | 79 | 1.0 | [32] |
| ZK60 | 72 | 2.8 | [33] |
| $Mg_{92}Zn_6Y_{1.5}Zr_{0.5}$ | 90 | 1.0 | [34] |
| $Mg_{97}Zn_1Y_2$ | 190 | 1.0 | Present study |

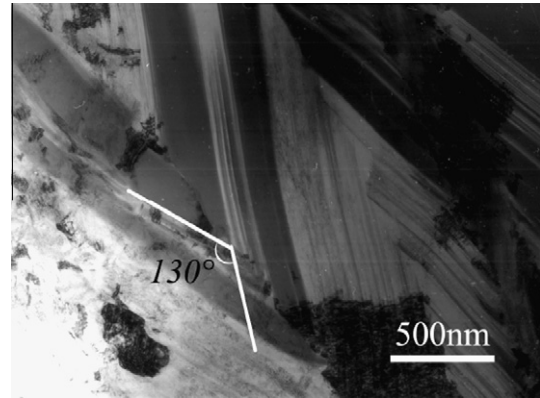


Fig. 14. TEM image showing kink bands with kinking angles much greater than 90° , without introducing fracture along the KBs in sample C.

ing in stage AB during compression (Fig. 1). And this might be the main reason why the peak stress (about 190 MPa) of the $Mg_{97}Zn_1Y_2$ alloy with a LPSO phase was higher than that of Mg alloys without LPSO structures (Table 2). In addition, it can be hypothesized that kinking of the LPSO block by a kinking angle θ can introduce a local plastic strain of about $1 - \cos(\theta/2)$. It was found that the kinking angle could be much higher than 90° without fracture along the KB (Fig. 14), which had not previously been observed in Mg alloys with other precipitates. The adjacent kink GBs in Mg were found to slide to accommodate such high angle KBs in the LPSO phase, without intergranular cracking (Fig. 14), relaxing large local strains and leading to relatively homogeneous plastic deformation. Therefore, kinking of the large LPSO blocks and its transplantation into the adjacent Mg grains resulted in extensive KBs and kink GBs in the alloy, as shown schematically by dotted ellipses in Fig. 15. Besides accommodating relatively large plastic deformation, the formation of multiple KBs and kink GBs results in refinement of the microstructure. Also, these newly formed boundaries will serve as obstacles to dislocation motion, so as to strengthen the alloy. Therefore, the formation of multiple KBs in the LPSO region and kink GBs in the bulk Mg grains is believed to be beneficial for the strength and ductility of the $Mg_{97}Zn_1Y_2$ alloy.

According to the Hall–Petch relationship a decrease in the width of the kink bands should result in further

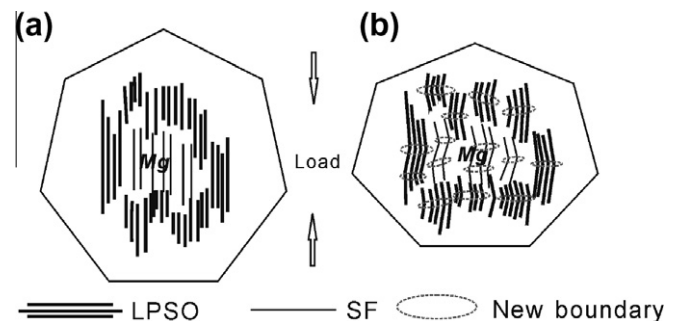


Fig. 15. Schematic illustration showing formation of multiple KBs and kink GBs. (a) As cast state. (b) Formation of KBs and kink GBs during deformation, denoted by dotted ellipses.

hardening of the $Mg_{97}Zn_1Y_2$ alloy, i.e. the compression curve should continue to ascend after point B (Fig. 1). However, work softening (stage BC, Fig. 1) was observed, which is in contradiction to the Hall–Petch prediction. There must be other deformation mechanisms responsible for the transition from work hardening to work softening with the occurrence of multiple kinking of the LPSO phase, which will be discussed in the next section.

4.3. Nucleation and propagation of microcracks in the LPSO phase

The fracture of metals is generally the result of the formation and propagation of microcracks. Few microcracks could be observed in the kinked LPSO region in sample B (Figs. 5 and 6). However, microcracks were found to nucleate in the interfaces of interlayer structures between the LPSO phase and Mg nano-slices at high angle KBs and propagate along the basal planes with the formation of multiple kink bands in sample C (Fig. 7). The measured stress kept on increasing in stage AB, but decreased in stage BC with increasing strain. This shows that the nucleation and propagation of microcracks within the sandwich structure of LPSO phase and Mg nano-slices could be a factor resulting in the decrease in flow stress in stage BC. According to the theory of elasticity, tensile stress resulting from the bending of lamellae is normal to the bent planes, i.e. the basal planes of the present LPSO phase. Thus it is not surprising that microcracks are always on the basal planes of the LPSO kink bands. It should be noted that there is a great difference in size between the bulk Mg grains and the Mg nano-slices embedded or sandwiched between the LPSO structures. This implies the formation extensive dislocations which are able to move in a large free volume over a path of several tens of micrometers in the Mg matrix [10], while the number and movement of dislocations in the Mg nano-slices embedded or sandwiched between LPSO layers was severely restricted (Fig. 6). When the number of dislocations exceeded the capability of the Mg nano-slices to accommodate them microcracks nucleated and propagated within the Mg nano-slice or along the interfaces, which could result in a decrease in flow stress. The work softening (stage BC, Fig. 1) could thus be attributed to the formation of microcracks and their propagation. However, the microhardness of the kinked LPSO phase in sample C was higher than that in sample B, while the flow stress continued to decrease after point “B” in the true strain–stress curve, which seems paradoxical. This is due to the fact that the microhardness test is less sensitive to tiny microcracks, compared with flow stress in the tensile or compressive test [35].

Stroh [36] showed that cleavage would be activated when:

$$\sigma_n \sigma_s \geq (k\gamma G)/(\alpha\pi) \quad (1)$$

where σ_n is the applied stress, σ_s is the resolved shear stress on the basal planes, k is a constant that depends on the elastic anisotropy of the crystal, γ is the surface energy of

the cleavage planes, G is the shear modulus and α is the length of a tilted KB. In this work cleavage, i.e. propagation of microcracks, would firstly take place in thicker LPSO blocks (where longer KB can be formed), according to Eq. (1). This theoretical prediction was verified by our experimental observations, as shown in Figs. 7 and 13. In Fig. 7 microcracks are observed at a KB located within the interlayer structure of the LPSO phase and Mg nano-slices, far from the LPSO phase–Mg matrix interface. However, no microcracks were observed at KBs close to the LPSO phase–Mg matrix interface in Fig. 13, where the LPSO structure is relatively thin according to the SEM observations (Figs. 2 and 4). Once a microcrack met a KB its propagation could be blocked (indicated by the white arrows in Fig. 7b), since the basal planes of the next kink band were deflected from the propagation direction due to multiple kinking, i.e. local cleavage of each kink band in the LPSO phase could occur but microcracks could not propagate easily into the neighboring kink band. This should be an advantage of layered structures. A well-known layered structure is the brick wall, where cracks in a piece of brick will not result in collapse of the wall. Therefore, it strongly suggests that formation of a second phase in a layered structure should be helpful in improving the ability to resist fracture of Mg alloys.

In addition, the kinking angle for the KBs immediately adjacent to the LPSO phase–Mg matrix interface ($\sim 26^\circ$) was usually much smaller than others further from the interface ($\sim 86^\circ$) (Fig. 13a). Correspondingly, no microcracks were observed at low angle KBs in the LPSO phase next to the LPSO phase–Mg matrix interface. The existence of a KB free of microcracks would certainly avoid cleavage of the kink band adjacent to the Mg grains and block the propagation of microcracks from the kinked LPSO structure into the Mg grains. This is also important for the ductility of the $Mg_{97}Zn_1Y_2$ alloy.

The formation of multiple kink bands can result in strengthening of the $Mg_{97}Zn_1Y_2$ alloy as a result of refinement, but the formation of microcracks leads to weakening. Thus, there is dynamic competition between strengthening and weakening during stage BC of deformation (Fig. 1). Work softening indicates that strengthening as a result of refinement of the LPSO phase by further kinking is insufficient to compensate for the weakening due to the formation and propagation of microcracks.

4.4. Effect of twinning and DRX on mechanical properties of the alloy

Twinning and DRX are usually reported to be dominant mechanisms which affect the deformation behavior of Mg alloys [28–30,37–39].

Deformation twinning in Mg alloys is generally activated at lower strains, which is one of the main sources of work hardening during the early stages of plastic deformation. It is known that $\{10\bar{1}2\}$ tensile twins and $\{10\bar{1}1\}$ and $\{10\bar{1}3\}$ compression twins can be formed during com-

pression in Mg alloys [40–42]. Unfortunately, cracks can nucleate at and propagate along $\{10\bar{1}2\}$ tensile twin boundaries [42]. Also, because compression twins induce a large shear deformation within the twin volume [41], cracking often takes place at their boundaries [40], which causes premature failure, i.e. although deformation twinning can strengthen Mg alloys during the early stages of plastic flow, twin boundaries will be weak points during the later stages of plastic deformation. Therefore, preventing the formation of deformation twins by microstructure control and/or optimizing the deformation conditions, i.e. the temperature and strain rate, in order to reduce the sites of nucleation of microcracks might be effective, improving the fracture toughness of Mg alloys. In the present $\text{Mg}_{97}\text{Zn}_1\text{Y}_2$ alloy the high density of basal SFs was found to strongly inhibit the formation of deformation twin (Fig. 12), with a consequent increase fracture toughness. In addition, the strongly anisotropic deformation behavior of the harder LPSO phase, as well as the strong and stable coherent LPSO phase–Mg matrix interface might play a role in reducing the occurrence of deformation twinning in adjacent Mg grains [12].

DRX is a result of rearrangement and/or annihilation of dislocations during high temperature deformation of Mg alloys, which can effectively lower the local stress concentration, as well as the flow stress. However, only a small volume fraction of recrystallized regions were observed in the present $\text{Mg}_{97}\text{Zn}_1\text{Y}_2$ alloy (Figs. 9–11), which is different from the large area DRXed region in the Mg matrix in extruded samples prepared at different high temperatures and by different processing techniques [26]. Therefore, little contribution of DRX to the deformation of this Mg alloy could be expected.

The lack of deformation twinning could reduce the number of potential nucleation sites for microcracks, which should be a key factor in obtaining high strain compression without fracture. Also, the limited fraction of DRX would not induce a significant decrease in flow stress during deformation. Both are possible reasons for the slight and slow work softening in stage BC up to a strain of 60%, rather than a rapid decrease in flow stress after the peak stress during deformation.

It is well known that there is dynamic competition between work softening due to DRX and work hardening (deformation twinning) in Mg grains, such as ZK60 [33] and $\text{Mg}_{92}\text{Zn}_6\text{Y}_{1.5}\text{Zr}_{0.5}$ [34], during the later stages of hot deformation, where there is a plateau in the stress–strain curve. In the present $\text{Mg}_{97}\text{Zn}_1\text{Y}_2$ alloy, however, hardening due to refinement of the LPSO phase by kinking, as well as work hardening in the Mg matrix, competed dynamically with softening, mainly due to microcracks in the LPSO structure during stage BC, since deformation twinning and DRX were not widely observed, in contrast to other Mg alloys [28,29,33,34].

Based on the above experimental results and discussions, it can be hypothesized that the present $\text{Mg}_{97}\text{Zn}_1\text{Y}_2$ alloy is a potential material for elevated temperature applications which will not fracture catastrophically for the fol-

lowing reasons: (i) refinement of the LPSO phase due to kinking, instead of coarsening, upon possible yielding; (ii) suppressed microcrack propagation by sub-KBs in the LPSO phase; and (iii) reduced nucleation sites for microcracks in the Mg matrix due to a limited number of deformation twins.

5. Conclusions

Based on microstructural investigations on a $\text{Mg}_{97}\text{Zn}_1\text{Y}_2$ alloy with a LPSO phase subjected to hot compression the influence of novel microstructures on the mechanical properties of the alloy was revealed. The following conclusions can be drawn:

1. The harder LPSO phase as well as the coherent LPSO phase–Mg matrix interface is beneficial for the strength and ability to resist fracture of Mg alloys.
2. Deformation kinking is important for both the strength and plasticity of the Mg alloy. Kinking of the LPSO phase could strengthen the alloy as a result of refinement. At the same time, kinking of the LPSO structure itself and its transplantation into the Mg matrix could afford considerable amount of plastic deformation to the material, which is important for the ductility of the alloy.
3. The formation of microcracks in the kinked interlayer structures of the LPSO phase and Mg nano-slices should be a factor in the work softening after the peak stress. However, their propagation could be restricted by KBs, which would also be helpful in ensuring the ductility and ability to resist premature fracture of the Mg alloy to some extent.
4. Deformation twins, which are potential cracking sites in Mg, are greatly reduced due to the existence of a high density of SFs with segregation of Zn/Y on the basal planes, which also plays a role in improving the mechanical properties. DRX makes only a minor contribution to work softening, since DRX is not widely observed in the present $\text{Mg}_{97}\text{Zn}_1\text{Y}_2$ alloy.
5. There is dynamic competition between strengthening (as a result of kinking in the LPSO phase and working hardening in the Mg matrix) and weakening (as a result of the formation of microcracks and DRX) during the later stages of deformation.

Acknowledgements

X.H.S. wishes to express appreciation to S.G. Wang of IMR for his help with sample preparation. This work was supported by the National Basic Research Program of China (2009CB623705).

References

- [1] Avedesian MM, Baker H. Magnesium and magnesium alloys. Materials Park (OH): ASM International; 1999.

- [2] Inoue A, Kawamura Y, Matsushita M, Hayashi K, Koike J. *J Mater Res* 2001;16:1894.
- [3] Kawamura Y, Hayashi K, Inoue A, Masumoto T. *Mater Trans* 2001;42:1172.
- [4] Abe E, Kawamura Y, Hayashi K, Inoue A. *Acta Mater* 2002;50:3845.
- [5] Chino Y, Mabuchi M, Hagiwara S, Iwasaki H, Yamamoto A, Tsubakino H. *Scripta Mater* 2004;51:711.
- [6] Itoi T, Seimiya T, Kawamura Y, Hirohashi M. *Scripta Mater* 2004;51:107.
- [7] Kawamura Y, Yamasaki M. *Mater Trans* 2007;48:2986.
- [8] Matsuda M, Ii S, Kawamura Y, Ikuhara Y, Nishida M. *Mater Sci Eng A* 2005;393:269.
- [9] Kawamura Y, Kasahara T, Izumi S, Yamasaki M. *Scripta Mater* 2006;55:453.
- [10] Matsuda M, Ando S, Nishida M. *Mater Trans* 2005;46:361.
- [11] Datta A, Waghmare UV, Ramamurty U. *Acta Mater* 2008;56:2531.
- [12] Matsuda M, Ii S, Kawamura Y, Ikuhara Y, Nishida M. *Mater Sci Eng A* 2004;386:447.
- [13] Hagihara K, Yokotani N, Kinoshita A, Sugino Y, Yamasaki M, Kawamura Y, et al. *MRS Symp Proc* 2009; 1128-U05-53.
- [14] Hagihara K, Yokotani N, Umakoshi Y. *Intermetallics* 2010;18:267.
- [15] Yoshimoto S, Yamasaki M, Kawamura Y. *Mater Trans* 2006;47:959.
- [16] Itoi T, Takahashi K, Moriyama H, Hirohashi M. *Scripta Mater* 2008;59:1155.
- [17] Li DJ, Zeng XQ, Dong J, Zhai CQ, Ding WJ. *J Alloys Compd* 2009;468:164.
- [18] Ping DH, Hono K, Kawamura Y, Inoue A. *Philos Mag Lett* 2002;82:543.
- [19] Suzuki M, Kimura T, Koike J, Maruyama K. *Mater Sci Eng A* 2004;387:706.
- [20] Yamasaki M, Sasaki M, Nishijima M, Hiraga K, Kawamura Y. *Acta Mater* 2007;55:6798.
- [21] Nie J, Oh-ishi K, Gao X, Hono K. *Acta Mater* 2008;56:6061.
- [22] Wang YF, Wang ZZ, Yu N, Zeng XQ, Ding WJ, Tang BY. *Scripta Mater* 2008;58:807.
- [23] Orawan E. *Nature* 1942;149:463.
- [24] Barsoum MW, Farber L, El-Raghy T. *Metall Mater Trans* 1999;30:1727.
- [25] Hess J, Barrett C. *Trans AIME* 1949;185:599.
- [26] Matsumoto R, Yamasaki M, Otsu M. *Mater Trans* 2009;50:841.
- [27] Tan J, Tan M. *Mater Sci Eng A* 2003;339:124.
- [28] Barnett M. *Mater Sci Eng A* 2007;464:1.
- [29] Barnett M. *Mater Sci Eng A* 2007;464:8.
- [30] Chino Y, Kado M, Mabuchi M. *Acta Mater* 2008;56:387.
- [31] Fatemi-Varzaneh S, Zarei-Hanzaki A, Haghshenas M. *Mater Sci Eng A* 2008;497:438.
- [32] Ishikawa K, Watanabe H, Mukai T. *Mater Lett* 2005;59:1511.
- [33] Galiyev A, Kaibyshev R, Gottstein G. *Acta Mater* 2001;49:1199.
- [34] Zhang Y, Zeng X, Lu C, Ding W. *Mater Sci Eng A* 2006;428:91.
- [35] Demers V, Brailovski V, Prokoshkin S, Inaekyan K. *J Mater Process Technol* 2009;209:3096.
- [36] Stroh A. *Philos Mag* 1958;3:625.
- [37] Liu Z, Bai S, Kang S. *Scripta Mater* 2008;60:403.
- [38] Myshlyaev M, McQueen H, Mwembela A, Konopleva E. *Mater Sci Eng A* 2002;337:121.
- [39] Xu S, Matsumoto N, Kamado S, Honma T, Kojima Y. *Scripta Mater* 2009;61:249.
- [40] Cizek P, Barnett M. *Scripta Mater* 2008;59:959.
- [41] Koike J. *Metall Mater Trans A* 2005;36:1689.
- [42] Somekawa H, Singh A, Mukai T. *Philos Mag Lett* 2009;89:2.